ATLAS NOTE

ATLAS-CONF-2014-051

September 25, 2014

Search for new phenomena in events with a photon and missing transverse momentum in pp collisions at $\sqrt{s} = 8$ TeV with the ATLAS detector

The ATLAS Collaboration

Abstract

Results of a search for new phenomena in events with an energetic photon and large missing transverse momentum with the ATLAS experiment at the LHC are reported. Data were collected in proton-proton collisions at a centre-of-mass energy of 8 TeV and correspond to an integrated luminosity of 20.3 fb^{-1}. The observed data are well described by the expected Standard Model backgrounds. The expected (observed) upper limit on the fiducial cross section for the production of $\gamma + E_{\mathrm{T}}^{\mathrm{miss}}$ events is 6.1 (5.3) fb at 95% CL. Exclusion limits are presented on models of new phenomena with dark matter candidates, large extra spatial dimensions, and supersymmetric quarks.

ATLAS-CONF-2014-051
25 September 2014

1 Introduction

Events that contain a high-momentum photon and large missing transverse momentum (referred to as $\gamma + E_{\mathrm{T}}^{\mathrm{miss}}$) comprise a low-background sample that provides powerful sensitivity to some models of new phenomena [1, 2, 3, 4, 5, 6, 7]. Theories with large extra spatial dimensions (*LED*), weakly interacting massive dark matter (*DM*) or supersymmetric (*SUSY*) partners of the quarks (squarks) in a compressed mass spectrum scenario predict the production of $\gamma + E_{\mathrm{T}}^{\mathrm{miss}}$ events in pp collisions beyond Standard Model (SM) expectations.

The model of LED proposed by Arkani-Hamed, Dimopoulos, and Dvali [8] (ADD) aims to solve the hierarchy problem by hypothesizing the existence of n additional spatial dimensions of size R, leading to a new fundamental scale M_D, where $M_{Planck}^2 \approx M_D^{2+n} R^n$. If these dimensions are compactified, a series of massive graviton modes results. These gravitons may be invisible to the ATLAS detector, but if the graviton is produced in association with a photon, the detector signature is a $\gamma + E_{\mathrm{T}}^{\mathrm{miss}}$ event; see Fig. 1a.

Though the presence of dark matter is well-established [9], its particle nature remains a mystery. A popular candidate is a weakly interacting massive particle (WIMP), denoted χ, which has an interaction strength with SM particles at the level of the weak interaction. If the WIMPs interact with quarks via a heavy mediator, they could be pair-produced in collider events. The $\chi\bar{\chi}$ pair would be invisible, but $\gamma + E_{\mathrm{T}}^{\mathrm{miss}}$ events can be produced via radiation of an initial-state photon in $q\bar{q}\chi\bar{\chi}$ interactions [10].

As observations so far do not provide strong constraints on the nature of the WIMPs and the theoretical framework to which they belong, it is particularly interesting to study model–independent effective field theories (EFT) with various forms of interaction between the WIMPs and the Standard Model particles[10]. In this framework, the mediator is effectively integrated out and the production mechanism at the LHC energy scale is considered as a contact interaction; see Fig. 1b. Several effective-field-theory operators are used as a representative set following the nomenclature of Ref. [10]: D5 (vector), D8 (axial-vector) and D9 (tensor), for which the WIMP is a Dirac fermion. The interactions of SM and DM particles are described by two parameters: the DM particle mass m_χ and the suppression scale (M_*) of the heavy mediator that is integrated out. In a UV-complete theory, the contact interaction would be replaced by an explicit mediator V; the suppression scale is linked to the mediator mass m_V by the relation $M_* = \sqrt{g_f g_\chi}$, where g_f and g_χ represent the coupling factors of the mediator to SM particles and WIMPs, respectively. However, as the typical momentum transfer in LHC collisions can reach the scale of the microscopic interaction, it is also crucial to probe specific models that involve the explicit production of the intermediate state, as shown in Fig. 1c. In this case, the interaction is effectively described by four parameters: m_χ, m_V, the width of the mediator Γ and the overall coupling $\sqrt{g_f g_\chi}$. In this paper, both the EFT approach presented in Ref. [10] and a specific model with a Z'–like mediator [11] are studied.

An alternative dark matter model hypothesizes interactions between the WIMPs and SM gauge bosons [12]. The effective coupling to different bosons is parameterized by k_1 and k_2, which control the coupling to the U(1) and SU(2) gauge sectors of the SM. In this model, dark matter production proceeds via $pp \to \gamma \to \gamma\chi\bar{\chi}$, requiring no initial-state radiation; see Fig. 1d. This model can also be used to describe the peak observed in the Fermi-LAT data [13], allowing for a direct comparison of Fermi and ATLAS data in the same parameter space.

Supersymmetry [14, 15, 16, 17, 18, 19, 20, 21, 22] postulates the existence of a new supersymmetric partner for each SM particle, with identical gauge couplings other than the difference of half a unit of spin. Collisions of protons could result in pair-production of squarks, $\tilde{q}$, which could decay to a SM quark and a neutralino $\tilde{\chi}_1^0$; the neutralino is assumed to be stable in R-parity conserving models [23]. If the mass difference $m_{\tilde{q}} - m_{\tilde{\chi}_1^0}$ is small, the SM quark would have very low momentum, giving a final state of only invisible particles. Again, the radiation of a photon either from an initial-state quark or an intermediate squark would result in $\gamma + E_{\mathrm{T}}^{\mathrm{miss}}$ events; see Fig. 1e.

The ATLAS [6] and CMS [7] collaborations have reported limits on possible models of new physics

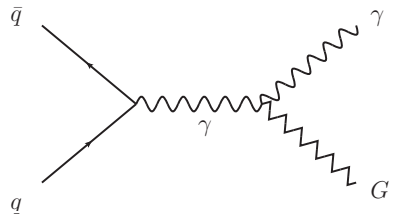

(a) Graviton production in models of large extra dimensions.

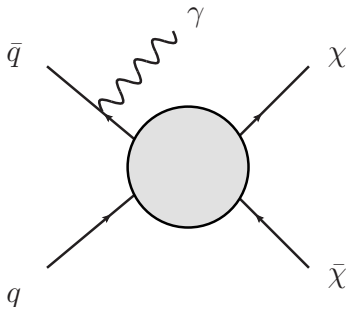

(b) Production of pairs of dark matter particles via an effective four-fermion $q\bar{q}\chi\bar{\chi}$ vertex.

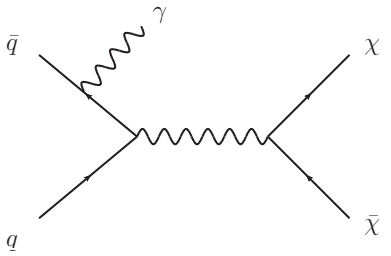

(c) Production of pairs of dark matter particles via an explicit s-channel mediator.

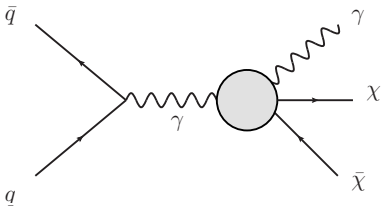

(d) Production of pairs of dark matter particles via an effective $\gamma\gamma\chi\bar{\chi}$ vertex.

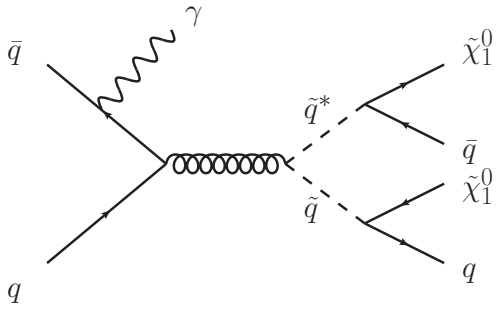

(e) Pair production of squarks ($\tilde{q}$), followed by decay into quarks and neutralinos ($\tilde{\chi}_1^0$).

Figure 1: Feynman diagrams depicting interactions that produce the $\gamma + E_{\mathrm{T}}^{\mathrm{miss}}$ final state.

based on searches for an excess in $\gamma + E_{\mathrm{T}}^{\mathrm{miss}}$ events using pp collisions at $\sqrt{s} = 7$ TeV. This paper reports the result of a search for new phenomena in $\gamma + E_{\mathrm{T}}^{\mathrm{miss}}$ events in pp collisions at $\sqrt{s} = 8$ TeV, collected by the ATLAS detector at the LHC in 2012.

2 The ATLAS detector

The ATLAS detector [24] is a multipurpose particle physics apparatus with a forward-backward symmetric cylindrical geometry and near 4π coverage in solid angle [25]. The inner tracking detector (ID) covers the pseudorapidity range $|\eta| < 2.5$, and consists of a silicon pixel detector, a silicon microstrip detector (SCT), and, for $|\eta| < 2.0$, a transition radiation tracker (TRT). The ID is surrounded by a thin superconducting solenoid providing a 2T magnetic field. A high-granularity lead/liquid-argon (LAr) sampling electromagnetic calorimeter covers the region $|\eta| < 3.2$. An iron/scintillator-tile calorimeter provides hadronic coverage in the range $|\eta| < 1.7$. LAr technology is also used for the hadronic calorimeters in the end-cap region $1.5 < |\eta| < 3.2$ and for both electromagnetic and hadronic measurements in the forward region up to $|\eta| < 4.9$. The muon spectrometer (MS) surrounds the calorimeters. It consists of three large air-core superconducting toroid systems, precision tracking chambers providing accurate muon tracking out to $|\eta| = 2.7$, and additional detectors for triggering in the region $|\eta| < 2.4$.

3 Event reconstruction

Photons are reconstructed from clusters of energy deposits in the electromagnetic calorimeter measured in projective towers. Clusters without matching tracks are classified as unconverted photon candidates. A photon is considered as a converted photon candidate if it is matched to a pair of tracks that pass a TRT hits requirement and that form a vertex in the ID that is consistent with coming from a massless particle, or if it is matched to a single track passing a TRT hits requirement and that has a first hit after the innermost layer of the pixel detector [26]. The photon energy in data is corrected by applying the energy scales measured with $Z \to e^+e^-$ decays and cross–checked with $J/\psi \to e^+e^-$ and $Z \to \ell\ell\gamma$ decays [27]. Identification requirements are applied in order to separate the photon candidates from the contamination coming from π^0 or other neutral hadrons decaying to two photons. The photon identification is based on the profile of the energy deposit in the first and second layer of the electromagnetic calorimeter. Photons have to pass the *tight* identification criteria of Ref. [28]. They are also required to be isolated, i.e, the energy in calorimeters in a cone of radius $\Delta R = \sqrt{(\Delta\eta)^2 + (\Delta\phi)^2} = 0.4$ around the cluster barycenter not associated with the photon cluster , is required to be less than 5 GeV. This cone energy is corrected for the leakage of the photon energy outside of the central core and for the soft energy deposits from multiple pp interactions in the same or neighboring bunch-crossings superimposed on the hard physics process (referred to as *pileup* interactions) [29].

Electrons are reconstructed from clusters in the electromagnetic calorimeter matched to a track in the ID and criteria for their identification and calibration procedure are similar to those used for photons. Electron candidates must satisfy the *medium++* identification requirement of Ref. [27]. Muons are identified either as a combined track in the MS and ID systems, or as an ID track which, once extrapolated to the MS, is associated with at least one track segment in the MS [30].

Jets are reconstructed using the anti-k_t algorithm [31, 32] with a radius parameter $R = 0.4$ from calibrated clusters of energy deposits in the calorimeters seeded by those with energies significantly above the measured noise. The differences in calorimeter response between electrons, photons and hadrons are taken into account by classifying each cluster, prior to the jet reconstruction, as coming from an electromagnetic or hadronic shower on the basis of its shape [33]. The jet energy thus accounts for electromagnetic and hadronic energy deposits at the cluster level with correction factors derived from Monte

Carlo simulation. A further correction, used to calibrate the jet energy to the scale of its constituent particles, (JES) [34, 35], is then applied. Jets are required to have transverse momentum $p_{\mathrm{T}} > 30$ GeV, $|\eta| < 4.5$ and a distance to the closest preselected electron or photon of $\Delta R > 0.2$.

The vector momentum imbalance in the transverse plane is obtained from the negative vector sum of the reconstructed and calibrated physics objects and is denoted as missing transverse momentum, $\boldsymbol{E}_{\mathrm{T}}^{\mathrm{miss}}$. The symbol $E_{\mathrm{T}}^{\mathrm{miss}}$ is used for its magnitude. Calorimeter energy deposits are associated with a reconstructed and identified high-transverse-momentum object in a specific order: electrons with $p_{\mathrm{T}} > 10$ GeV, photons with $p_{\mathrm{T}} > 10$ GeV and jets with $p_{\mathrm{T}} > 20$ GeV. Deposits not associated with any such objects are also taken into account in the $E_{\mathrm{T}}^{\mathrm{miss}}$ calculation [36] using an energy-flow algorithm that considers calorimeter energy deposits as well as ID tracks [37].

4 Event selection

The data have been collected in pp collisions at $\sqrt{s} = 8$ TeV. Events are selected using an $E_{\mathrm{T}}^{\mathrm{miss}}$ trigger that requires a missing transverse momentum greater than 80 GeV [38]. Events selected using an e/γ trigger with a threshold of $p_{\mathrm{T}}^{e} > 120$ GeV are also used in some control regions as described below [39]. Only data taken during periods where the calorimeters, ID and MS were well-functioning are considered. The data used correspond to an integrated luminosity of 20.3 fb^{-1}. Quality requirements are applied to photon candidates in order to reject those arising from instrumental problems. In addition, quality requirements are applied in order to remove jets arising from detector noise and out-of-time energy deposits in the calorimeter from cosmic rays or other non-collision sources [40]. Events are required to have a reconstructed primary vertex with at least 5 associated tracks.

The criteria for selecting events in the signal region (SR) are optimized to have a good acceptance for the squark model and the dark matter model with a Z'-like mediator, as well as to suppress the background from SM processes. This signal region also provides good sensitivity to the other models described above. Events in the SR are required to have $E_{\mathrm{T}}^{\mathrm{miss}} > 150$ GeV, a photon with high transverse momentum $p_{\mathrm{T}}^{\gamma} > 125$ GeV and $|\eta| < 1.37$ not overlapped in azimuth with $\boldsymbol{E}_{\mathrm{T}}^{\mathrm{miss}}$: $\Delta\phi(\gamma,\boldsymbol{E}_{\mathrm{T}}^{\mathrm{miss}}) > 0.4$. Events with more than one jet with $p_{\mathrm{T}} > 30$ GeV or with a jet with $\Delta\phi(\mathrm{jet},\boldsymbol{E}_{\mathrm{T}}^{\mathrm{miss}}) < 0.4$ are rejected. Events with one jet are retained to increase the signal acceptance and reduce systematic uncertainties related to the modeling of initial-state radiation. Events are required to have no electron ($p_{\mathrm{T}} > 7$ GeV, $|\eta| < 2.47$) and no muon ($p_{\mathrm{T}} > 6$ GeV, $|\eta| < 2.5$). The lepton veto mainly rejects W/Z events with charged leptons in the final state. For events satisfying these criteria, the $E_{\mathrm{T}}^{\mathrm{miss}}$ trigger efficiency is 0.99 ± 0.01, as determined using events selected with the e/γ trigger. The final data sample contains 521 events, where 319 and 202 events have zero and one jet respectively.

5 Monte Carlo simulation samples

Monte Carlo (MC) simulated samples are used to estimate the signal acceptance, the detector efficiency and to help in the estimation of the SM background contributions.

Simulated signal samples for ADD models are generated with Pythia8 [41] version 1.7.5 using the parton distribution function (PDF) MSTW2008LO [42] and a photon $p_{\mathrm{T}}^{\mathrm{min}} = 80$ GeV with $M_D = 2.0, 2.5$ TeV and the number of extra-dimension, n, varied from 2 to 6.

Simulated samples of dark matter production $pp \to \gamma + \chi\bar{\chi}$ via the $qq\chi\bar{\chi}$ interaction are generated using Madgraph5 [43] version 1.4.8.4 requiring $p_{\mathrm{T}}^{\gamma} > 120$ GeV, with showering and hadronisation modeled by Pythia8 version 1.6.5 using the AU2 tune [44]; the MSTW2008LO PDFs are used. Values of m_{χ} from 1 to 1300 GeV are considered. In addition, simulated samples of $pp \to \gamma + \chi\bar{\chi}$ are produced using the simplified model with a Z'-like mediator [11] using the same simulation programs as for the

effective-field-theory samples. Again, a photon with $p_{\mathrm{T}}^{\gamma} > 120$ GeV is required at parton-level. Both vector and axial vector couplings are considered. For each value of the mediator mass m_V, two different values of the mediator width are simulated: $\Gamma = m_V/8\pi$ and $\Gamma = m_V/3$. The lower value corresponds to a mediator that can annihilate into only one quark flavor and helicity and has unit couplings; it can be regarded as an approximate lower limit on the mediator width. A value of $\Gamma = m_V/3$ is a reasonable upper bound for a narrow resonance approximation.

Samples of $pp \to \gamma + \chi\bar{\chi}$ are also produced via the $\gamma\gamma\chi\bar{\chi}$ interaction model [12] with a fermionic WIMP. These samples are generated with MADGRAPH5 version 1.4.2 for a WIMP mass of 130 GeV and over a grid of values of k_1 and k_2, which are the theoretical parameters that control the relative couplings of the WIMPs to gauge bosons.

Simulated samples of $pp \to \tilde{q}\tilde{q}^*\gamma \to q\bar{q}\gamma + \tilde{\chi}_1^0\tilde{\chi}_1^0$ are generated by MADGRAPH5 version 1.5.11 with showering and hadronisation modeled by PYTHIA6 [45] version 4.2.7 and CTEQ6L1 PDF [46], with the requirement of having one photon at parton-level with $p_{\mathrm{T}}^{\gamma} > 80$ GeV and $|\eta| < 2.5$. Only the first two generations of squarks are considered, and they are assumed to be degenerate in mass. Signal cross sections are calculated to next-to-leading order in the strong coupling constant including the resummation of soft gluon emission at next-to-leading-logarithmic accuracy (NLO+NLL) when available [47, 48, 49, 50, 51]. The nominal cross section and the uncertainty are taken from an envelope of cross section predictions using different PDF sets and factorisation and renormalisation scales, as described in Ref. [52].

Simulated samples of $Z\gamma$ and $W\gamma$ events are generated with SHERPA version 1.4.1 [53], with parton-level requirements of $p_{\mathrm{T}}^{\gamma} > 70$ GeV and $p_{\mathrm{T}}^{\gamma} > 80$ GeV, respectively, and invariant dilepton mass $m_{\ell\ell} > 40$ GeV. A sample of simulated γ + jet events is generated with PYTHIA8 version 1.6.5. The W/Z + jet processes are also simulated using SHERPA version 1.4.1 with massive b/c-quarks. Diboson samples are generated with HERWIG [54] version 6.520, the single top samples with MC@NLO [55] version 4.06 for s-channel and Wt production, or ACERMC [56] version 3.8 for t-channel production. Simulated samples of top-quark pair production are generated by POWHEG [57] version r2129. The W/Z + jet, diboson and top samples are only used as a cross check.

HERWIG version 6.520 is used for simulating the parton shower and fragmentation processes in combination with JIMMY [58] for underlying event simulation for the MC@NLO samples, while PYTHIA version 6.426 is used for the POWHEG and ACERMC samples. The proton PDFs used are CTEQ6L1 [46] for the PYTHIA8 and ACERMC samples, and CT10 [59] for the MC@NLO, SHERPA and POWHEG samples. The ATLAS underlying event tune AUET2 [44] is used, except for the $t\bar{t}$ sample that uses the new Perugia 2011C tune [60]. SHERPA uses its own parton shower, fragmentation and underlying event model.

Differing pileup conditions as a function of the instantaneous luminosity are taken into account by overlaying simulated minimum-bias events generated with PYTHIA8 onto the hard-scattering process and re-weighting them according to the distribution of the average number of interactions observed.

The simulated samples are processed either with a full ATLAS detector simulation [61] based on GEANT4 [62] or a fast simulation based on the parameterization of the response of the electromagnetic and hadronic showers in the ATLAS calorimeters [63] and a simulation of the trigger system. The results based on fast simulation are validated against fully simulated samples. The simulated events are reconstructed and analyzed with the same analysis chain as for the data, using the same trigger and event selection criteria discussed above.

6 Background estimation

The SM background to the $\gamma + E_{\mathrm{T}}^{\mathrm{miss}}$ final state is dominated by the $Z(\to \nu\nu) + \gamma$ process, where the photon is due to initial-state radiation. Secondary contributions come from $W\gamma$ and $Z\gamma$ production with unidentified electrons, muons or hadronically decaying τ leptons, or W/Z production where a lepton or an associated radiated jet is misidentified as a photon. In addition, there are smaller contributions from

top-quark pair production, diboson, γ+jet and multijet production.

6.1 $Z\gamma$ and $W\gamma$ backgrounds

The $E_{\mathrm{T}}^{\mathrm{miss}}$-dependence of events due to $Z\gamma$ and $W\gamma$ backgrounds is described using simulated samples, while the normalisation is obtained via a likelihood fit to observed yields in several control regions (CR), constructed to be enriched in specific backgrounds. Poisson likelihood functions are used for event counts in all regions; the systematic uncertainties described below are treated as Gaussian-distributed nuisance parameters in the likelihood function. Key ingredients of the fit are the normalisation scale factors for the $W\gamma$ and $Z\gamma$ processes, which enable observations in the CRs to constrain background estimates in the SR. The same normalisation factor is used for $Z(\nu\nu) + \gamma$, $Z(\mu\mu) + \gamma$ and $Z(ee) + \gamma$. Three control regions are defined by inverting lepton vetoes. In the first control region, the $W\gamma$ contribution is enhanced by requiring the presence of a muon. The second (third) control regions enhance the $Z\gamma$ background by requiring the presence of a pair of muons (electrons). In the muon control regions, muons are treated as invisible particles and are not considered in the $\boldsymbol{E}_{\mathrm{T}}^{\mathrm{miss}}$ computation. As the signal region definition includes a veto on the presence of muons, this $\boldsymbol{E}_{\mathrm{T}}^{\mathrm{miss}}$ definition ensures that the control regions have a similar $E_{\mathrm{T}}^{\mathrm{miss}}$ spectrum as the signal region. The same procedure is followed for electrons in the electron control regions, by adding the transverse momentum of the electrons to the missing transverse momentum vector thereby removing the electron contribution to the calculation of $E_{\mathrm{T}}^{\mathrm{miss}}$. In each case, the CR lepton selection follows the same requirements as the SR lepton veto with the additional requirements that the lepton must be associated with an isolated track and that $\Delta R(\ell, \gamma) > 0.5$. In addition, the photon pseudorapidity requirement is relaxed with respect to the SR selection: $|\eta| < 2.37$, excluding the calorimeter crack region $1.37 < |\eta| < 1.52$, to increase the number of events in the CR. For both the $Z\gamma$-enriched control regions, the dilepton mass $m_{\ell\ell}$ is required to be greater than 50 GeV. The normalisation of the dominant $Z\gamma$ background process is largely constrained by the event yields in the two $Z(\rightarrow \ell^+\ell^-)\gamma$ control regions. The results are cross-checked using the transfer-factor technique employed in the previous ATLAS analysis of the $\gamma + E_{\mathrm{T}}^{\mathrm{miss}}$ final state [6]; the two methods give consistent results.

6.2 Fake photons from misidentified electrons

Contributions from processes in which an electron is misidentified as a photon are estimated by scaling yields from a sample of $e + E_{\mathrm{T}}^{\mathrm{miss}}$ events by an electron-to-photon misidentification factor. This factor is measured from mutually exclusive samples of e^+e^- and $\gamma + e$ events. To establish a pure sample of electrons, m_{ee} and $m_{e\gamma}$ are both required to be consistent with the Z boson mass, and the multijet background is subtracted making use of sideband estimates. The misidentification factor is parametrized as a function of E_{T} in three pseudorapidity bins. Similar estimates are made for the three control regions, scaling event yields from samples matching the control region requirements, but requiring an electron rather than a photon.

6.3 Fake photons from misidentified jets

Background contributions from events in which a jet is misidentified as a photon are estimated by extrapolating from samples of $\gamma + E_{\mathrm{T}}^{\mathrm{miss}}$ events where the photon has failed isolation requirements. The yield in this sample is scaled by a jet-to-photon misidentification factor, after subtraction of the contribution from real photons. The jet-to-photon misidentification factor is measured in samples enriched in jets, selected by inverting the photon identification criteria, and is determined from the ratio of jets that are isolated or non-isolated. This estimation accounts also for the contribution from multijets, which can mimic the monophoton signature if one jet is misreconstructed as a photon and one or more other jet is

badly reconstructed resulting in large fake $E_{\mathrm{T}}^{\mathrm{miss}}$. The multijet background is found to be negligible in the SR.

6.4 γ + jet background

The γ + jet background contribution to the signal region originates if the jet is badly reconstructed and partially lost, creating fake $E_{\mathrm{T}}^{\mathrm{miss}}$. Despite the large production rate, this process is only a minor source of background as it is suppressed by the large $E_{\mathrm{T}}^{\mathrm{miss}}$ and the large jet-$E_{\mathrm{T}}^{\mathrm{miss}}$ separation requirements in the SR. This background is estimated from MC simulation and is cross-checked with a data-driven estimation, which gives a result in agreement with the MC simulation, but is limited by a large statistical uncertainty. The data-driven estimation is derived from a control region defined by requiring all the selection criteria of the SR but reversing the $\Delta\phi(\text{jet},\boldsymbol{E}_{\mathrm{T}}^{\mathrm{miss}})$ requirement, thereby selecting poorly reconstructed events in which the jet is aligned to the $\boldsymbol{E}_{\mathrm{T}}^{\mathrm{miss}}$. Simulated samples are used to estimate and subtract electroweak backgrounds coming from W/Z + jet and $Z/W + \gamma$ processes. As events with a jet with $p_{\mathrm{T}} > 30$ GeV and that are not well-separated from $\boldsymbol{E}_{\mathrm{T}}^{\mathrm{miss}}$ are vetoed in the SR selection, the γ + jet and multijet contribution in the SR is then estimated with a linear extrapolation of the jet p_{T} spectrum in this CR to the $p_{\mathrm{T}} < 30$ GeV region.

6.5 Final estimation and systematic uncertainties

Background estimates in the SR are first derived from a fit using only data from the leptons CRs, in order to assess the consistency of the observed SR yield with the background model. The values of the normalisation factors for the $W\gamma$ and $Z\gamma$ backgrounds, obtained from the fit to the CRs, are $k_{W\gamma} = 0.81 \pm 0.05 \pm 0.06$ and $k_{Z\gamma} = 0.89 \pm 0.08 \pm 0.08$, where the uncertainties are statistical followed by systematic. Distributions of the missing transverse momentum in the three control regions are shown in Figs. 2, 3, and 4.

The techniques used for the background estimation are checked in a validation region, where events are selected with the same criteria used for the signal region, except for a lower $E_{\mathrm{T}}^{\mathrm{miss}}$ (110−150 GeV) and a larger photon pseudorapidity ($|\eta| < 2.37$) to increase the statistical power. To suppress the background from γ + jet and from fake photons to a level similar to that in the SR, a requirement on the azimuthal separation between the photon and the jet – when there is a jet in the event – is applied: $\Delta\phi(\gamma, \text{jet}) < 2.7$. To minimize the contamination of signal events in this region, a requirement on the azimuthal separation between the photon and $E_{\mathrm{T}}^{\mathrm{miss}}$ is added: $\Delta\phi(\gamma,\boldsymbol{E}_{\mathrm{T}}^{\mathrm{miss}}) < 3.0$. The number of events in data in this region is 307 and the estimated total background, obtained from the background-only fit to the control regions, is $272 \pm 17(\text{stat.}) \pm 14(\text{syst.})$, resulting in an agreement between data and expectation within 2σ. Detailed results are shown in Table 1; systematic uncertainties are computed as described below for the SR.

Systematic uncertainties on the background predictions in the signal region are presented here in terms of the relative uncertainty to the total background prediction from the CR fit, which provides constraints on many of the sources of systematic uncertainty. The dominant contribution is due to the uncertainty on the electron fake rate, which contributes a 4.6% relative uncertainty and to the reconstruction and identification efficiency corrections on electrons and muons applied in MC simulation, which contribute 1.3% and 0.7% relative uncertainty, respectively. The uncertainty in the absolute electron/photon energy scale translates into a 0.6% relative uncertainty on the total background prediction. Uncertainties in the simulation of the electron/photon energy resolution, isolation, and identification efficiency contribute a relative uncertainty of 0.1% to the total predicted background. The uncertainty on the absolute jet energy scale [35] and the jet energy resolution [64] contribute 0.1% and 0.5% relative uncertainties, respectively. Uncertainties on the scale and resolution of the calorimeter energy deposits not associated with high-p_{T} physics objects affect the calculation of the $E_{\mathrm{T}}^{\mathrm{miss}}$ and generate an uncertainty of 0.3% on the background prediction. Uncertainties in the PDF are evaluated by following, for the CT10 and

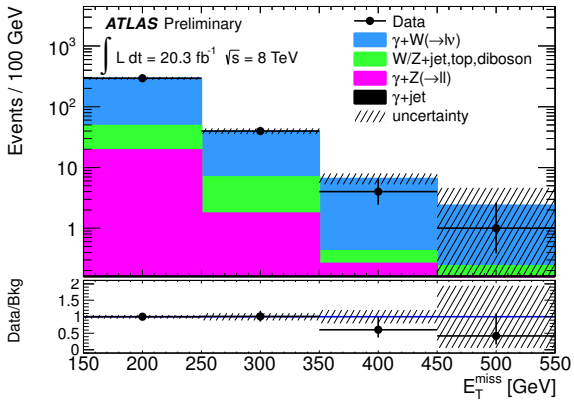

Figure 2: Distribution of $E_{\mathrm{T}}^{\mathrm{miss}}$ in the data and for the expected background in the single-muon control region. The total background expectation has been normalized to the observed number of events in this control region. Overflows are included in the final bin. The lower part of the figure shows the ratio of event yields in the data and background expectation.

MSTW2008LO PDF sets, the PDF4LHC recommendations [65]. The Hessian method is used to obtain asymmetric uncertainties at 68% CL. To obtain also inter-PDF uncertainties, results are then compared with those obtained with the NNPDF set. Renormalisation and factorisation scale uncertainties are also taken into account by increasing and decreasing the scales used in the MC generators by a factor of two. PDF and scale uncertainties contribute 0.7% to the background prediction uncertainty. Additional sources of systematic uncertainty, due to the trigger requirement, the 2.8% relative uncertainty on the integrated luminosity, derived by following the same methodology as that detailed in Ref. [66], and the pileup modeling described above, introduce a combined relative uncertainty of less than 0.1%.

The final total background prediction systematic uncertainty of about 5%, while the statistical uncertainty is about 6%.

7 Results

In Table 1, the observed number of events and the SM background predictions obtained from a fit to CRs are presented. The $E_{\mathrm{T}}^{\mathrm{miss}}$ distribution in the SR is shown in Fig. 5.

Table 1: Predicted event yield in the signal region (SR) and the validation region (VR) from SM backgrounds, using estimates and uncertainties obtained from a fit in the control regions. Uncertainties are statistical followed by systematic.

Process	Event yield (SR)	Event yield (VR)
$Z(\rightarrow \nu\nu) + \gamma$	$389 \pm 36 \pm 10$	$153 \pm 16 \pm 10$
$W(\rightarrow \ell\nu) + \gamma$	$82.5 \pm 5.3 \pm 3.4$	$67 \pm 5 \pm 5$
W/Z + jet, $t\bar{t}$, diboson	$83 \pm 2 \pm 28$	$47 \pm 2 \pm 14$
$Z(\rightarrow \ell\ell) + \gamma$	$2.0 \pm 0.2 \pm 0.6$	$2.9 \pm 0.3 \pm 0.6$
γ + jet	$0.4^{+0.3}_{-0.4}$	$2.5^{+4.0}_{-2.5}$
Total background	$557 \pm 36 \pm 27$	$272 \pm 17 \pm 14$
Data	521	307

As the 521 events observed in data are well described by the SM background prediction of $557 \pm 36 \pm 27$, the results are interpreted in terms of exclusions on models that would produce an excess of

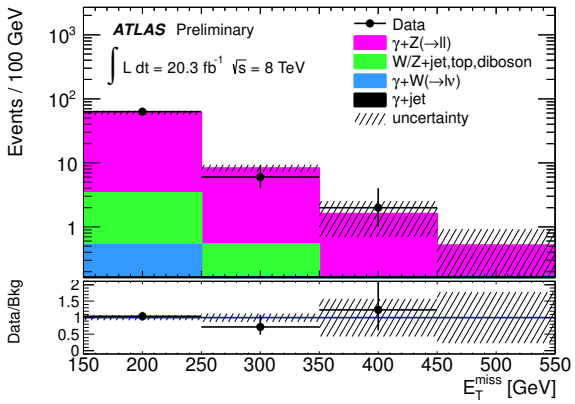

Figure 3: Distribution of $E_{\mathrm{T}}^{\mathrm{miss}}$ in the data and for the expected background in the two-muon control region. The total background expectation has been normalized to the observed number of events in this control region. Overflows are included in the final bin. The lower part of the figure shows the ratio of event yields in the data and background expectation.

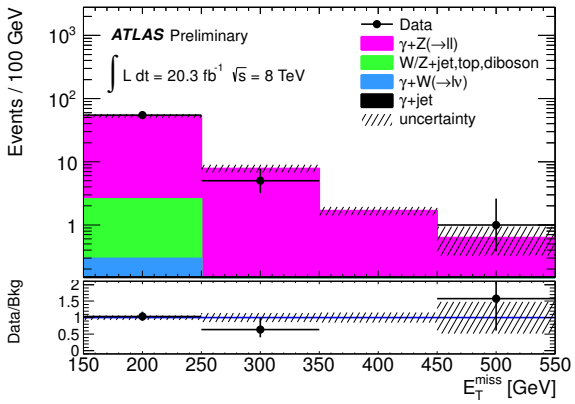

Figure 4: Distribution of $E_{\mathrm{T}}^{\mathrm{miss}}$ in the data and for the expected background in the two-electron control region. The total background expectation has been normalized to the observed number of events in this control region. Overflows are included in the final bin. The lower part of the figure shows the ratio of event yields in the data and background expectation.

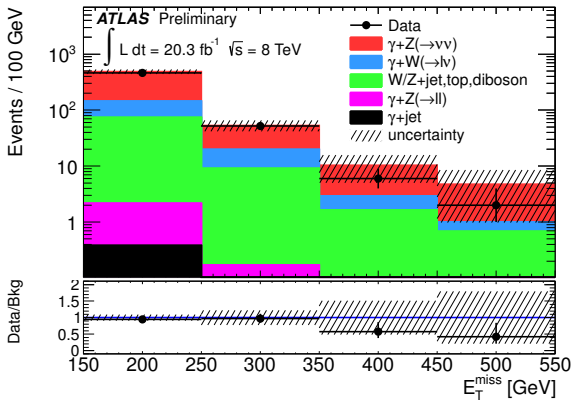

Figure 5: Distribution of $E_{\mathrm{T}}^{\mathrm{miss}}$ in the data and for the background in the signal region predicted from the fit in the CRs. Overflows are included in the final bin. The lower part of the figure shows the ratio of event yields in the data and background expectation.

$\gamma + E_{\mathrm{T}}^{\mathrm{miss}}$ events. Upper bounds are calculated using a one-sided profile likelihood ratio and the CLs technique [67, 68], evaluated using the asymptotic approximation [69] on data from the CRs as well as from the SR.

The most model-independent limits provided are those on the fiducial cross section, $\sigma \times A$. The fiducial acceptance A is defined using a selection identical to that defining the signal region but applied at particle level, were the particle-level $E_{\mathrm{T}}^{\mathrm{miss}}$ is the vector sum of invisible particle momenta. The limit on $\sigma \times A$ is derived from a limit on the visible cross section $\sigma \times A \times \epsilon$, where ϵ is the fiducial reconstruction efficiency. A conservative estimate $\epsilon = 69\%$ is computed using ADD and WIMP samples with no quark/gluon produced from the main interaction vertex. The expected (observed) upper limit on the fiducial cross section is 6.1 (5.3) fb at 95% CL and 5.1 (4.4) fb at 90% CL. These limits are applicable to any model that produces $\gamma + E_{\mathrm{T}}^{\mathrm{miss}}$ events in the fiducial region and has similar reconstruction efficiency ϵ.

In the case of limits on specific models, the impact of systematic uncertainties on signal samples is evaluated separately on $A \times \epsilon$ (PDF, scale, initial-state radiation (ISR), final-state radiation (FSR)), and the cross section σ (PDF and scale uncertainties). Only uncertainties affecting $A \times \epsilon$ are included in the statistical analysis; uncertainties affecting the cross section are indicated as bands on observed limits and written as σ_{theo}. For the EFT and the simplified model dark matter samples, scale uncertainties are evaluated by varying the renormalisation, factorisation and matching scales in MADGRAPH by a factor 0.5 and 2. For the ADD samples, the PYTHIA8 renormalisation and factorisation scale parameters are varied independently to 0.5 and 2.0. For these samples, the ISR and FSR signal uncertainties are assessed by varying the PYTHIA8 parameters, as done in Ref. [70]. For the squark model, systematic uncertainties arising from the treatment of ISR/FSR are studied with MC data samples by varying the value of α_s, renormalisation and factorisation scales and the MADGRAPH/PYTHIA matching parameters. Radiation uncertainties are typically less than 10%, PDF uncertainties less than 30%, scale uncertainties less than 20%.

Limits on dark matter production are derived from the cross–section limits at a given WIMP mass m_χ, and expressed as 90% CL limits on the suppression scale M_*, for the D5 (Fig. 6), D8 (Fig. 7) and D9 (Fig. 8) operators. M_* values up to 760, 760 and 1010 GeV are excluded for the D5, D8 and D9 operators, respectively. As already mentioned, the effective field theory becomes a poor approximation when the momentum transferred in the interaction, Q_{tr}, is comparable to the mass of the intermediate state $m_V = M_* \sqrt{g_f g_\chi}$ [10, 71], In order to illustrate the sensitivity to the unknown ultraviolet completion of the theory, limits computed retaining only simulated events with $Q_{\mathrm{tr}} < m_V$ are also shown, for a value of the coupling $\sqrt{g_f g_\chi}$ either unity or the maximum value (4π) that allows the perturbative regime to be valid. This procedure is referred to as *truncation*. As can be seen in Figs 6, 7 and 8, the truncated limits nearly overlap the non-truncated limits for a 4π coupling; for unit coupling, the truncated limits are less stringent than the non-truncated limits at low m_χ, and the analysis loses sensitivity for $m_\chi > 100$ (200) GeV for the D5 and D8 (D9) operators. These lower limits on M_* can be translated into upper limits on the nucleon-WIMP interaction cross section as a function of m_χ using Eq. (4) and (5) of Ref. [10]. Results are shown in Fig. 9 for spin-independent (D5) and spin-dependent (D8, D9) DM-nucleon interactions and are compared to measurements from various dark matter search experiments [72, 73, 74, 75, 76, 77, 78, 79, 80, 81, 82, 83, 84]. The search for dark matter pair production in association with a γ at the LHC allows for the extension of the limits on the χ-nucleon scattering cross section in the low mass region $m_\chi < 10$ GeV where the astroparticle experiments have less sensitivity due to the very low-energy recoils such low-mass dark matter particles would induce.

Simplified models with explicit mediators are ultraviolet complete and therefore robust for all values of Q_{tr}. For the simplified Z'-like model with vector interactions and mediator width $\Gamma = m_V/3$, Fig. 10 shows the 95% CL limits on the coupling parameter $\sqrt{g_f g_\chi}$ calculated for various values of the WIMP and mediator particle masses, and compared to the lower limit resulting from the relic DM abundance

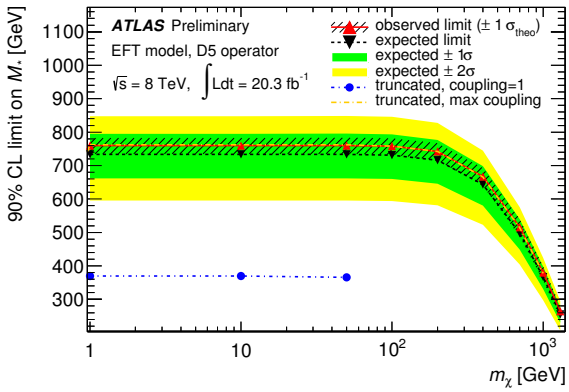

Figure 6: Limits at 90% CL on the EFT suppression scale M_* as a function of the WIMP mass m_χ, for vector operator D5. Results where EFT truncation has been applied (see text) are also shown, assuming coupling values $\sqrt{g_f g_\chi} = 1, 4\pi$. For unit coupling, the analysis has no sensitivity for $m_\chi \geq 100$ GeV; as no sample was generated between $m_\chi = 50$ GeV and $m_\chi = 100$ GeV, the limit is only shown up to $m_\chi = 50$ GeV. For 4π coupling, the truncated limit nearly overlaps the non-truncated limit.

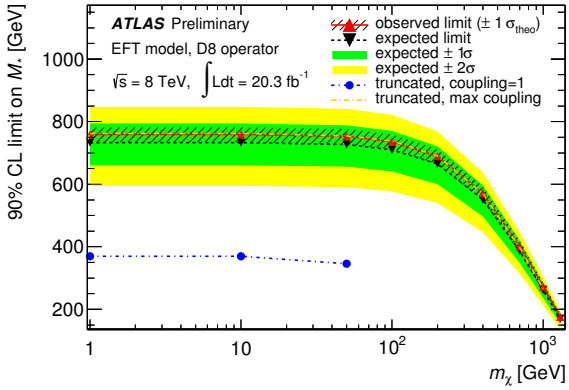

Figure 7: Limits at 90% CL on the EFT suppression scale M_* as a function of the WIMP mass m_χ, for axial-vector operator D8. Results where EFT truncation has been applied (see text) are also shown, assuming coupling values $\sqrt{g_f g_\chi} = 1, 4\pi$. For unit coupling, the analysis has no sensitivity for $m_\chi \geq 100$ GeV; as no sample was generated between $m_\chi = 50$ GeV and $m_\chi = 100$ GeV, the limit is only shown up to $m_\chi = 50$ GeV. For 4π coupling, the truncated limit nearly overlaps the non-truncated limit.

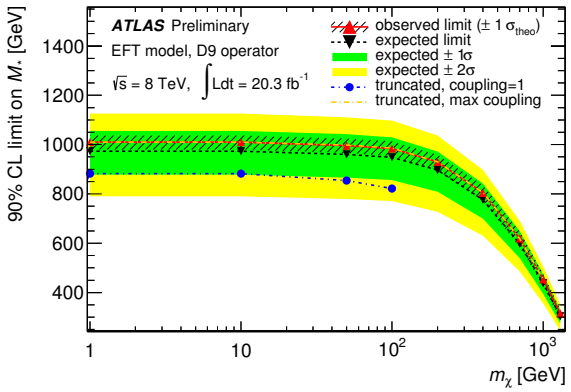

Figure 8: Limits at 90% CL on the EFT suppression scale M_* as a function of the WIMP mass m_χ, for tensor operator D9. Results where EFT truncation has been applied (see text) are also shown, assuming coupling values $\sqrt{g_f g_\chi} = 1, 4\pi$. For unit coupling, the analysis has no sensitivity for $m_\chi > 200$ GeV; as no sample was generated between $m_\chi = 100$ GeV and $m_\chi = 200$ GeV, the limit is only shown up to $m_\chi = 100$ GeV. For 4π coupling, the truncated limit nearly overlaps the non-truncated limit.

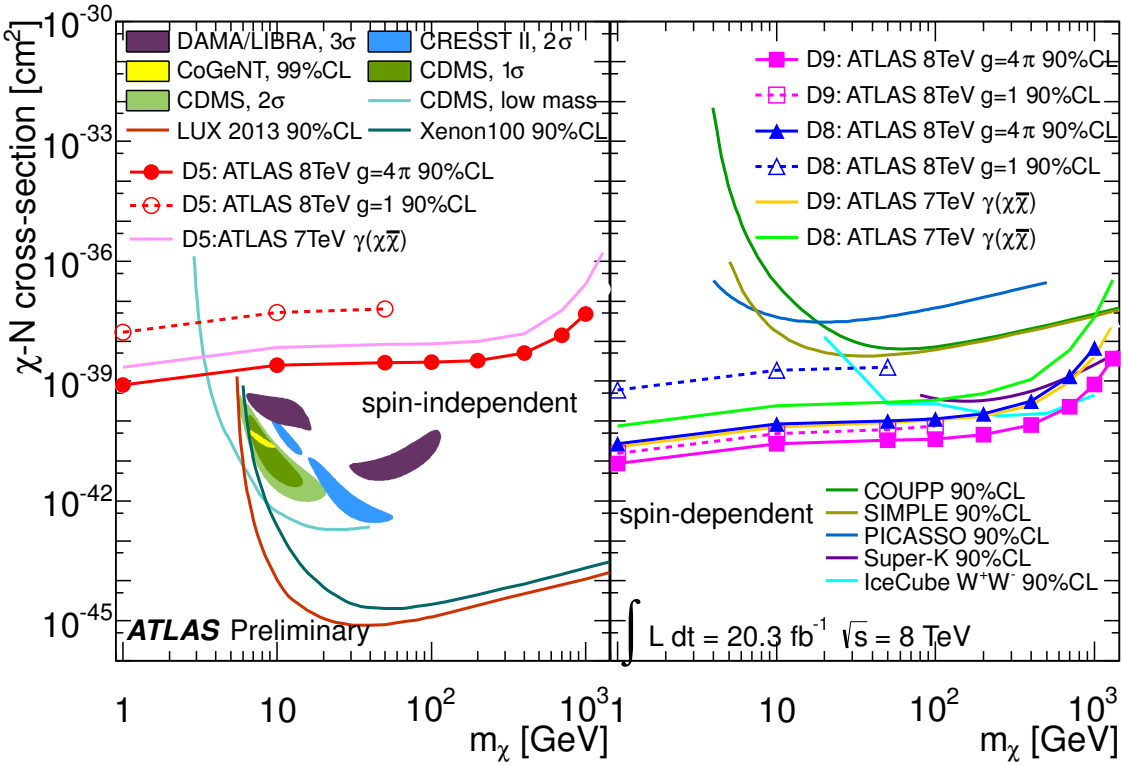

Figure 9: Upper limits at 90% CL on the nucleon-WIMP cross section as a function of m_χ for spin-independent (left) and spin-dependent (right) interactions, for the cases that the coupling is unity or that the coupling is the maximum ($g = 4\pi$) allowed to keep the model within its perturbative regime. The truncation procedure is applied for both cases. The results obtained from ATLAS with 7 TeV data for the same channel are shown for comparison. Also shown are results from various dark matter search experiments [72, 73, 74, 75, 76, 77, 78, 79, 80, 81, 82, 83, 84].

[85]. Fig. 11 and 12 show, for vector and axial–vector interactions and different values of the WIMP mass, the corresponding 95% CL limits on the suppression scale M_* as a function of m_V. One can note how, when the mediator mass is greater than the LHC reach, the EFT model provides a good approximation of the simplified model with $M_* = m_V/\sqrt{g_f g_\chi}$. The truncation procedure is applied when computing the EFT limits; these limits are always more conservative than those from the simplified model as long as m_V is greater than or equal to the value used for EFT truncation. This can be seen by comparing the M_* limits derived from the EFT approach using validity truncation (Figs. 6 and 7), recalling $m_V = \sqrt{g_f g_\chi} M_*$.

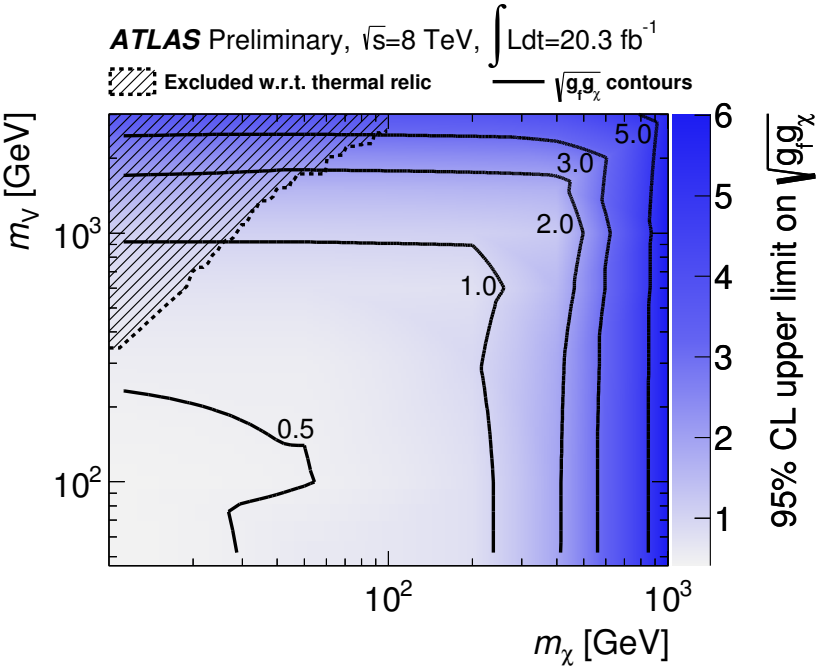

Figure 10: 95% CL limits on the WIMP simplified model coupling parameter with vector coupling and mediator width $\Gamma = m_V/3$, as a function of the WIMP (m_χ) and the mediator particle masses (m_V). Solid lines indicate contours in the coupling parameter. In the region above the dashed line, the lower limits on the coupling resulting from the relic abundance of DM are higher than the upper limits found in this analysis.

In the case of the model of $\gamma\gamma\chi\bar{\chi}$ interactions with an s-channel SM gauge boson, inspired by the line in the Fermi-LAT γ-ray spectrum, limits are placed on the effective mass scale M_* in the (k_1,k_2) parameter plane; see Fig. 13. The exclusion line is drawn by considering the value of M_* needed to generate the $\chi\bar{\chi} \to \gamma\gamma$ annihilation rate consistent with the observed Fermi-LAT γ-ray line. This analysis is able to constrain effectively the parameter space of the theory compatible with the Fermi-LAT peak.

In the ADD model of LED, limits on M_D for various values of n are provided in Fig. 14. Results incorporating truncation are also shown, for which the graviton production cross section is suppressed by a factor $M_D^4/\hat{s}^2$, where $\sqrt{\hat{s}}$ is the parton-parton centre-of-mass energy. The analysis is able to exclude M_D up to 2.17 TeV, depending on the number of extra dimensions. The effect of truncation is larger for higher n as the graviton mass distribution is pushed to higher values.

In the case of squark pair production, limits are presented on $\sigma(pp \to \tilde{q}\tilde{q}^*\gamma)$ as a function of $m_{\tilde{q}}$ and $m_{\tilde{q}} - m_{\tilde{\chi}_1^0}$; see Fig. 15. The limit is presented down to $m_{\tilde{q}} - m_{\tilde{\chi}_1^0} = m_c$, below which the decay of the $\tilde{c} \to c\tilde{\chi}_1^0$ is offshell and not considered here. For very compressed spectra, the analysis is able to exclude

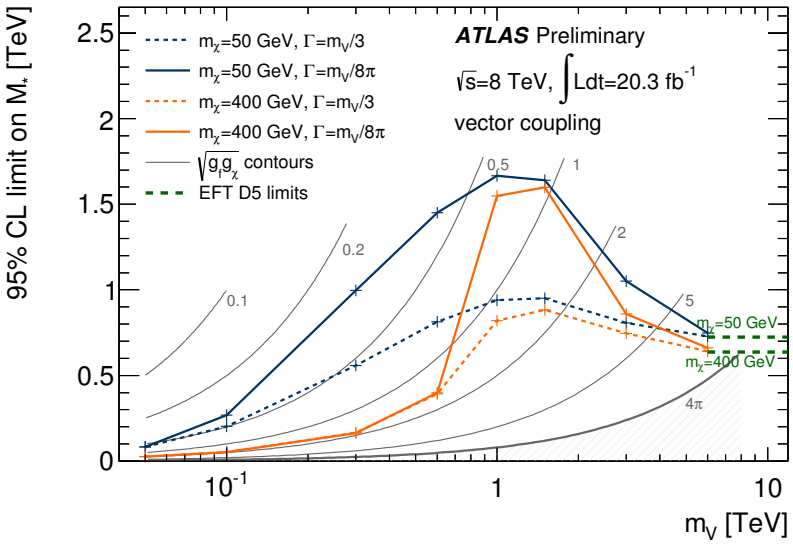

Figure 11: 95% observed limits on the EFT suppression scale M_* as a function of the mediator mass m_V, for a Z'–like mediator with vector interactions. For a dark matter mass m_χ of 50 or 400 GeV, results are shown for different values of the mediator total decay width Γ and compared to the EFT observed limit results for a D5 (vector) interaction. M_* vs m_V contours for a total coupling $\sqrt{g_f g_\chi} = 0.1, 0.2, 0.5, 1, 2, 5, 4\pi$ are also shown. At high m_V, the model approaches that of a contact interaction, which can be seen to agree with the corresponding limits from the D5 operator shown as a dashed line.

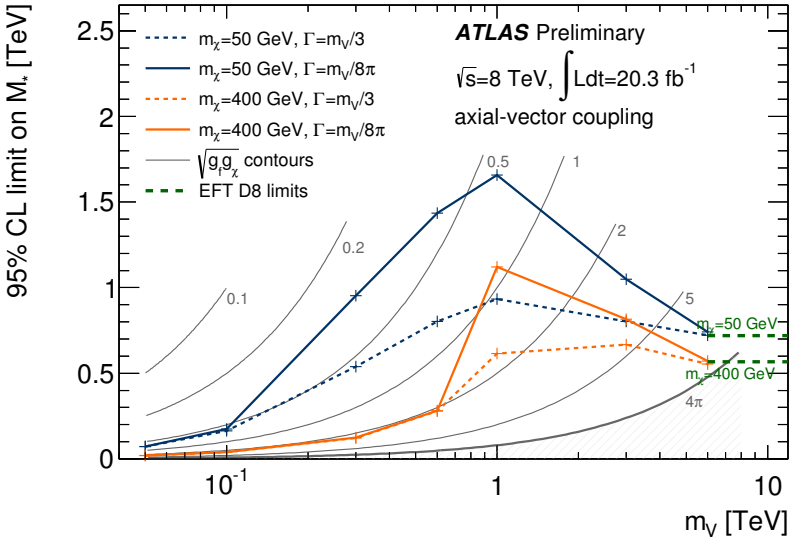

Figure 12: 95% observed limits on the EFT suppression scale M_* as a function of the mediator mass m_V, for a Z'–like mediator with axial-vector interactions. For a dark matter mass m_χ of 50 or 400 GeV, results are shown for different values of the mediator total decay width Γ and compared to the EFT observed limit results for a D8 (axial-vector) interaction. M_* vs m_V contours for a total coupling $\sqrt{g_f g_\chi} = 0.1, 0.2, 0.5, 1, 2, 5, 4\pi$ are also shown. At high m_V, the model approaches that of a contact interaction, which can be seen to agree with the corresponding limits from the D8 operator shown as a dashed line.

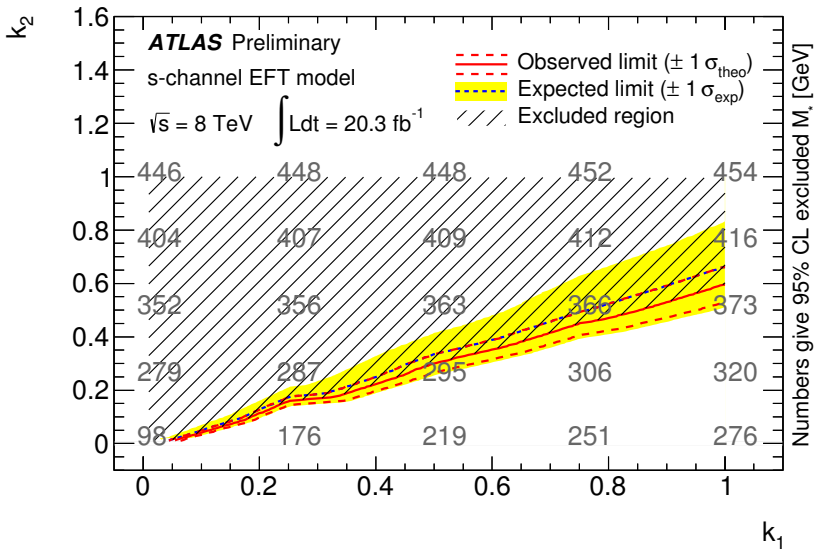

Figure 13: 95% CL limits on the effective mass scale M_* in the (k_2,k_1) parameters plane for the s-channel EFT model inspired by Fermi-LAT for $m_\chi = 130$ GeV. The k_1, k_2 parameters control the couplings of the dark matter particles to electroweak bosons as defined in Ref. [12]. The exclusion line is drawn by considering the proper annihilation rate to give the observed yield in the Fermi-LAT γ-ray line. The upper part of the plane is excluded.

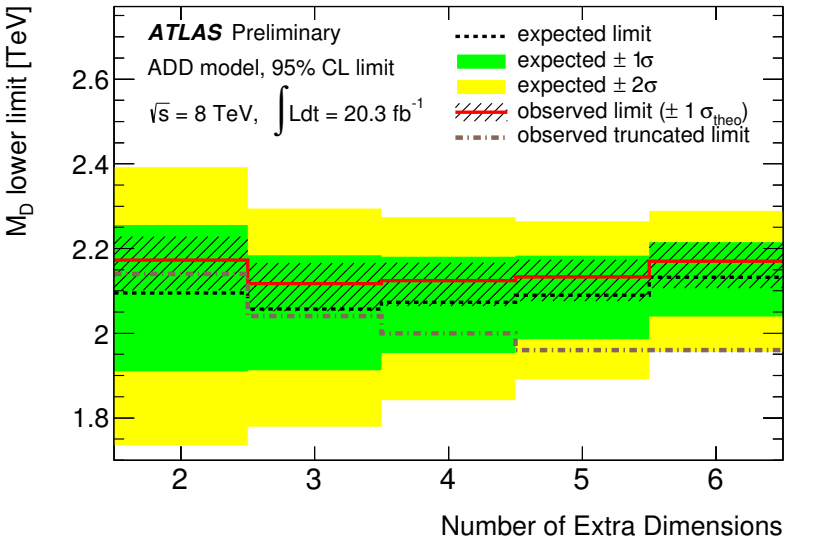

Figure 14: Lower limits at 95% CL on the mass scale M_D in the ADD models of large extra dimensions, for several values of n, the number of extra dimensions. The expected and observed limits are shown, along with the limit obtained after applying truncation.

squark masses up to 250 GeV. Some models of first and second generation squark pair production are also explored in Ref. [86]; the result presented here is complementary in that it probes very compressed spectra. Due to the reduced hadronic activity, the acceptance of the $\gamma + E_{\mathrm{T}}^{\mathrm{miss}}$ selection indeed increases as the mass difference between the squarks and the neutralino decreases, leading to an increased sensitivity to squark mass with decreasing mass difference.

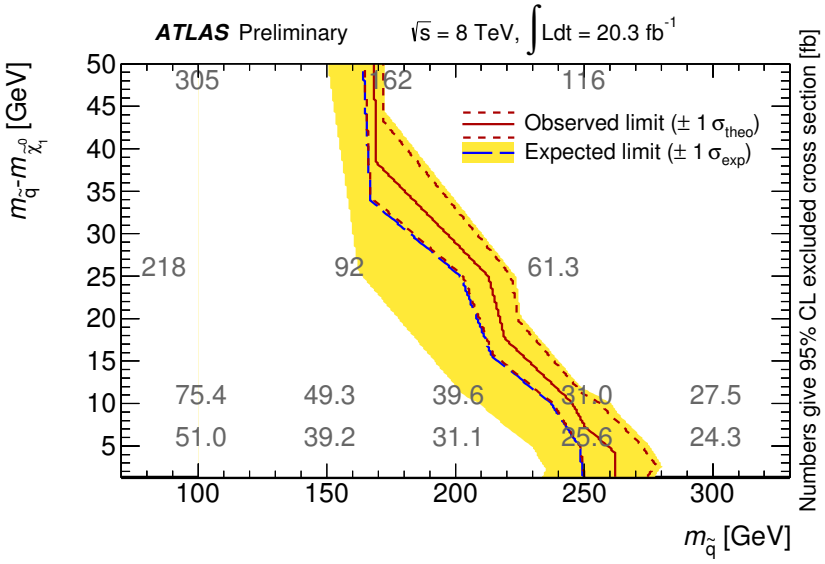

Figure 15: Upper limits at 95% CL on the cross section for the compressed squark model, as a function of $m_{\tilde{q}}$ and $m_{\tilde{q}} - m_{\tilde{\chi}_1^0}$, in the compressed region $m_{\tilde{q}} - m_{\tilde{\chi}_1^0} < 50$ GeV. The observed (solid line) and expected (dashed line) upper limits from this analysis are shown; the upper limit on the cross-section (in fb) is indicated for each model point.

8 Summary

Results are reported for the search for new phenomena in events with a high transverse-momentum photon and large missing transverse momentum in pp collisions at $\sqrt{s} = 8$ TeV at the LHC, using ATLAS data corresponding to an integrated luminosity of 20.3 fb^{-1}. The observed data are in agreement with the SM background prediction. The expected (observed) upper limits on the fiducial cross section $\sigma \times A$ are 6.1 (5.3) fb at 95% CL and 5.1 (4.4) fb at 90% CL. In addition, limits are placed on parameters of theories of large extra dimensions, WIMP dark matter and supersymmetric quarks.

References

[1] CDF Collaboration, T. Aaltonen et al., Phys.Rev.Lett. **101** (2008) 181602, arXiv:0807.3132 [hep-ex].

[2] D0 Collaboration, V. Abazov et al., Phys.Rev.Lett. **101** (2008) 011601, arXiv:0803.2137 [hep-ex].

[3] OPAL Collaboration, G. Abbiendi et al., Eur.Phys.J. **C18** (2000) 253–272, arXiv:hep-ex/0005002 [hep-ex].

[4] L3 Collaboration, P. Achard et al., Phys.Lett. **B587** (2004) 16–32, arXiv:hep-ex/0402002 [hep-ex].

[5] DELPHI Collaboration, J. Abdallah et al., Eur.Phys.J. **C38** (2005) 395–411, arXiv:hep-ex/0406019 [hep-ex].

[6] ATLAS Collaboration, Phys.Rev.Lett. **110** (2013) 011802, arXiv:1209.4625 [hep-ex].

[7] CMS Collaboration, Phys.Rev.Lett. **108** (2012) 261803, arXiv:1204.0821 [hep-ex].

[8] N. Arkani-Hamed, S. Dimopoulos, and G. Dvali, Phys.Lett. **B429** (1998) 263–272, arXiv:hep-ph/9803315 [hep-ph].

[9] G. Bertone, D. Hooper, and J. Silk, Phys.Rept. **405** (2005) 279–390, arXiv:hep-ph/0404175 [hep-ph].

[10] J. Goodman, M. Ibe, A. Rajaraman, W. Shepherd, T. M. Tait, et al., Phys.Rev. **D82** (2010) 116010, arXiv:1008.1783 [hep-ph].

[11] P. J. Fox, R. Harnik, J. Kopp, and Y. Tsai, Phys. Rev **D 85** (2011) 056011, arXiv:1109.4398 [hep-ph].

[12] A. Nelson, L. M. Carpenter, R. Cotta, A. Johnstone, and D. Whiteson, Phys. Rev. **D 89** (2014) 056011, arXiv:1307.5064 [hep-ph].

[13] C. Weniger, JCAP **1208** (2012) 007, arXiv:1204.2797 [hep-ph].

[14] H. Miyazawa, Prog. Theor. Phys. **36 (6)** (1966) 1266–1276.

[15] P. Ramond, Phys. Rev. **D3** (1971) 2415–2418.

[16] Y. A. Golfand and E. P. Likhtman, JETP Lett. **13** (1971) 323–326. [Pisma Zh. Eksp. Teor. Fiz. 13:452-455,1971].

[17] A. Neveu and J. H. Schwarz, Nucl. Phys. **B31** (1971) 86–112.

[18] A. Neveu and J. H. Schwarz, Phys. Rev. **D4** (1971) 1109–1111.

[19] J. Gervais and B. Sakita, Nucl. Phys. **B34** (1971) 632–639.

[20] D. V. Volkov and V. P. Akulov, Phys. Lett. **B46** (1973) 109–110.

[21] J. Wess and B. Zumino, Phys. Lett. **B49** (1974) 52.

[22] J. Wess and B. Zumino, Nucl. Phys. **B70** (1974) 39–50.

[23] P. Fayet, Phys. Lett. B **64** (1976) 159.

[24] ATLAS Collaboration, JINST **3** (2008).

[25] ATLAS uses a right-handed coordinate system with its origin at the nominal interaction point (IP) in the center of the detector and the z-axis along the beam pipe. The x-axis points from the IP to the center of the LHC ring, and the y-axis points upward. Cylindrical coordinates (r, ϕ) are used in the transverse plane, ϕ being the azimuthal angle around the beam pipe. The pseudorapidity is defined in terms of the polar θ angle as $\eta = -\ln[\tan(\theta/2)]$.

[26] ATLAS Collaboration, Report No. ATLAS-CONF-2010-005 (2010). https://cds.cern.ch/record/1273197.

[27] ATLAS Collaboration, arXiv:1407.5063v1 [hep-ex]. (Accepted by EPJC).

[28] ATLAS Collaboration, Report No. ATLAS-CONF-2012-123, (2012). https://cds.cern.ch/record/1473426/.

[29] ATLAS Collaboration, Phys.Rev. **D83** (2011) 052005, arXiv:1012.4389 [hep-ex].

[30] ATLAS Collaboration, arXiv:1407.3935 [hep-ex].

[31] M. Cacciari, G. P. Salam, and G. Soyez, JHEP **04** (2008) 063, arXiv:0802.1189 [hep-ph].

[32] M. Cacciari and G. P. Salam, Phys. Lett. **B641** (2006) 57–61, arXiv:hep-ph/0512210.

[33] ATLAS Collaboration, Eur.Phys.J. **C73** (2013) 2304, arXiv:1112.6426 [hep-ex].

[34] ATLAS Collaboration, Eur. Phys. J. **C73 3** (2013) 2304, arXiv:1112.6426 [hep-ex].

[35] ATLAS Collaboration, arXiv:1203.1302 [hep-ex].

[36] ATLAS Collaboration, Report No. ATLAS-CONF-2013-082, (2013). https://cds.cern.ch/record/1570993.

[37] ATLAS Collaboration, Eur. Phys. J. **C72** (2012) 1844, arXiv:1108.5602 [hep-ex].

[38] ATLAS Collaboration, Report No. ATLAS-CONF-2014-02, (2014). https://cds.cern.ch/record/1647616.

[39] ATLAS Collaboration, Report No. ATLAS-CONF-2012-048, (2012). https://cds.cern.ch/record/1450089/.

[40] ATLAS Collaboration, Report No. ATLAS-CONF-2012-020, (2012). https://cds.cern.ch/record/1430034.

[41] T. Sjostrand, S. Mrenna, and P. Z. Skands, Comput.Phys.Commun. **178** (2008) 852–867, arXiv:0710.3820 [hep-ph].

[42] A. Martin, W. Stirling, R. Thorne, and G. Watt, Eur. Phys. J. **C63** (2009) 189–285, arXiv:0901.0002 [hep-ph].

[43] J. Alwall, M. Herquet, F. Maltoni, O. Mattelaer, and T. Stelzer, JHEP **1106** (2011) 128, arXiv:1106.0522 [hep-ph].

[44] ATLAS Collaboration, Report No. ATLAS-PHYS-PUB-2011-008 (2011). https://cds.cern.ch/record/1345343.

[45] T. Sjostrand, S. Mrenna, and P. Skands, JHEP **05** (2006) 026, arXiv:hep-ph/0603175.

[46] J. Pumplin et al., JHEP **0207** (2002) 012, arXiv:hep-ph/0201195 [hep-ph].

[47] W. Beenakker, R. Hopker, M. Spira, and P. Zerwas, Nucl.Phys. **B492** (1997) 51–103, arXiv:hep-ph/9610490 [hep-ph].

[48] A. Kulesza and L. Motyka, Phys.Rev.Lett. **102** (2009) 111802, arXiv:0807.2405 [hep-ph].

[49] A. Kulesza and L. Motyka, Phys.Rev. **D80** (2009) 095004, arXiv:0905.4749 [hep-ph].

[50] W. Beenakker, S. Brensing, M. Kramer, A. Kulesza, E. Laenen, et al., JHEP **0912** (2009) 041, arXiv:0909.4418 [hep-ph].

[51] W. Beenakker, S. Brensing, M. Kramer, A. Kulesza, E. Laenen, et al., Int.J.Mod.Phys. **A26** (2011) 2637–2664, arXiv:1105.1110 [hep-ph].

[52] M. Kramer, A. Kulesza, R. van der Leeuw, M. Mangano, S. Padhi, et al., arXiv:1206.2892 [hep-ph].

[53] T. Gleisberg et al., JHEP **0902** (2009) 007, arXiv:0811.4622 [hep-ph].

[54] G. Corcella et al., JHEP **0101** (2001) 010, arXiv:hep-ph/0011363 [hep-ph].

[55] S. Frixione and B. R. Webber, JHEP **0206** (2002) 029, arXiv:hep-ph/0204244 [hep-ph].

[56] B. P. Kersevan and E. Richter-Was, arXiv:hep-ph/0405247 [hep-ph].

[57] S. Frixione, P. Nason, and G. Ridolfi, JHEP **0709** (2007) 126, arXiv:hep-ph/0707.3088.

[58] J. Butterworth, J. R. Forshaw, and M. Seymour, Z. Phys. **C72** (1996) 637–646, arXiv:hep-ph/9601371 [hep-ph].

[59] H.-L. Lai et al., Phys. Rev. **D82** (2010) 074024, arXiv:1007.2241 [hep-ph].

[60] B. Cooper, J. Katzy, M. L. Mangano, A. Messina, L. Mijović, and P. Skands, arXiv:1109.5295 [hep-ph].

[61] ATLAS Collaboration, Eur. Phys. J. **C70** (2010) 823–874, arXiv:1005.4568 [physics.ins-det].

[62] GEANT4 Collaboration, S. Agostinelli et al., Nucl. Instrum. Meth. **A506** (2003) 250–303.

[63] ATLAS Collaboration, Report No. ATLAS-PHYS-PUB-2010-013, (2010). https://cds.cern.ch/record/1300517.

[64] ATLAS Collaboration, Report No. ATLAS-CONF-2010-054, (2010). https://cds.cern.ch/record/1281311.

[65] M. Botje et al., arXiv:1101.0538 [hep-ph].

[66] ATLAS Collaboration, arXiv:1302.4393 [hep-ex]. (Submitted to EPJC).

[67] A. L. Read, J. Phys. G **G28** (2002) 2693–2704.

[68] T. Junk, Nucl.Instrum.Meth. **A434** (1999) 435–443, arXiv:hep-ex/9902006 [hep-ex].

[69] G. Cowan, K. Cranmer, E. Gross, and O. Vitells, Eur. Phys. J. **C71** (2011) 1554, arXiv:1007.1727 [physics.data-an].

[70] ATLAS Collaboration, arXiv:1404.0051 [hep-ex].

[71] G. Busoni, A. De Simone, E. Morgante, and A. Riotto, Phys.Lett. **B728** (2014) 412–421, arXiv:1307.2253 [hep-ph].

[72] XENON100 Collaboration, Phys. Rev. Lett. **109** (2012) 181301, arXiv:1207.5988 [astro-ph.CO].

[73] CDMS Collaboration, Phys. Rev. Lett. **106** (2011) 131302, arXiv:1011.2482 [astro-ph.CO].

[74] CoGeNT Collaboration, Phys. Rev. Lett. **106** (2011) 131301, arXiv:1002.4703 [astro-ph.CO].

[75] PICASSO Collaboration, Phys. Lett. B **711** (2012) 153–161, arXiv:1202.1240 [hep-ex].

[76] M. Felizardo et al., Phys. Rev. Lett. **108** (2012) 201302, arXiv:1106.3014 [astro-ph.CO].

[77] LUX Collaboration, D. S. Akerib et al., Phys. Rev. Lett. **112** (2014) 091303.

[78] Super-Kamiokande Collaboration, S. Desai et al., Phys.Rev. **D70** (2004) 083523, arXiv:hep-ex/0404025 [hep-ex].

[79] IceCube Collaboration, M. G. Aartsen et al., Phys. Rev. Lett. **110** (2013) 131302, arXiv:arXiv:1212.4097 [astro-ph.HE].

[80] COUPP Collaboration, E. Behnke et al., Phys. Rev. D **86** (2012) 052001, arXiv:arXiv:1204.3094 [astro-ph.CO].

[81] G. Angloher, M. Bauer, I. Bavykina, A. Bento, C. Bucci, et al., Eur.Phys.J. **C72** (2012) 1971, arXiv:1109.0702 [astro-ph.CO].

[82] CDMS Collaboration, R. Agnese et al., Phys.Rev.Lett. **111** (2013) 251301, arXiv:1304.4279 [hep-ex].

[83] DAMA Collaboration, R. Bernabei et al., Eur.Phys.J. **C56** (2008) 333–355, arXiv:0804.2741 [astro-ph].

[84] HESS Collaboration, A. Abramowski et al., Phys.Rev.Lett. **110** (2013) 041301, arXiv:1301.1173 [astro-ph.HE].

[85] WMAP Collaboration, E. Komatsu et al., Astrophys.J.Suppl. 192 (2011), arXiv:arXiv:1001.4538 [astro-ph.CO].

[86] ATLAS Collaboration, arXiv:1405.7875 [hep-ex].

9 Auxiliary Material

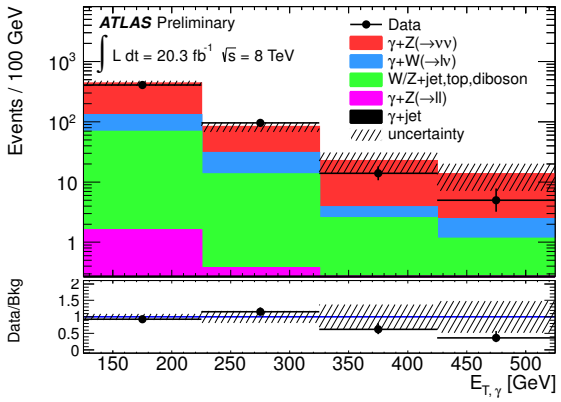

Figure 16: Distribution of $E_{T,\gamma}$ in the data and for the expected background in the signal region predicted from the fit in the CRs. The lower part of the figure shows the ratio of events yields in the data and background expectation.

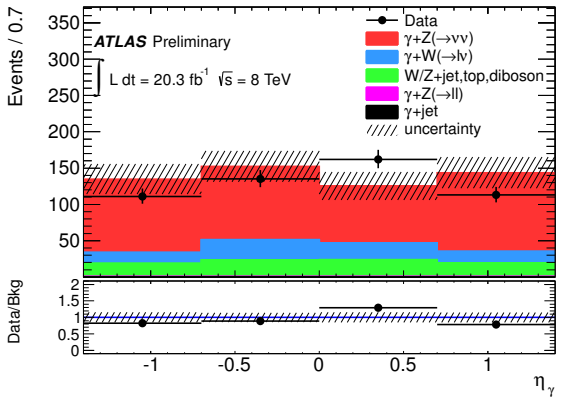

Figure 17: Distribution of η_γ in the data and for the expected background in the signal region predicted from the fit in the CRs. The lower part of the figure shows the ratio of events yields in the data and background expectation.

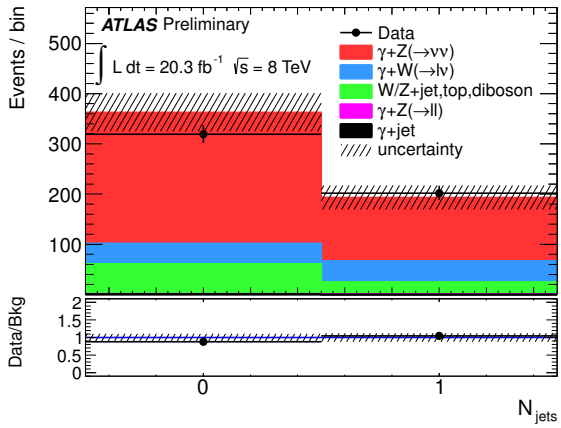

Figure 18: Distribution of N_{jet} in the data and for the expected background in the signal region predicted from the fit in the CRs. The lower part of the figure shows the ratio of events yields in the data and background expectation.

Cut	**Weighted**
Nominal (after skimming)	6944.49
Pre-selected:	
1. GRL	6944.49
2. Trigger	6652.86
3. Good vertex	6645.7
4. Event cleaning	6645.7
5. Jet cleaning	6625.9
6. $E_{\mathrm{T}}^{\mathrm{miss}}$cleaning	6365.87
SR Cuts:	
1.$E_{\mathrm{T}}^{\mathrm{miss}}$> 150 GeV	3671.55
2. At least one loose photon with p_{T}> 125 GeV($\|\eta\| < 2.37$)	2645.02
3. The leading photon is tight with $\|\eta\| < 1.37$	2068.26
4. The leading photon is isolated	1898.19
5. $\Delta\phi(\gamma^{leading}, E_{\mathrm{T}}^{\mathrm{miss}})$ >0.4	1887.16
6. Jet veto:$N_{\mathrm{jet}} \leq 1$ and $\Delta\phi$(jet, $E_{\mathrm{T}}^{\mathrm{miss}}$) >0.4	1218.62
7. Lepton veto	1187.92

Table 2: Example cutflow for the compressed squark signal point with $m_{\tilde{q}} = 200$ GeVand $m_{\tilde{\chi}_1^0} = 195$ GeV. 10000 events were generated.